# Supplementary Information for Adaptive optical quantitative phase imaging based on annular illumination Fourier ptychographic microscopy

**Yefeng Shu[1,2,3,†], Jiasong Sun[1,2,3,†], Jiaming Lyu[4], Yao Fan[1,2,3], Ning Zhou[1,2,3], Ran Ye[1,5], Guoan Zheng[6*], Qian Chen[1,2,3,*], and Chao Zuo[1,2,3,*]**

[1]Smart Computational Imaging (SCI) Laboratory, Nanjing University of Science and Technology, Nanjing, Jiangsu Province 210094, China
[2]Smart Computational Imaging Research Institute (SCIRI) of Nanjing University of Science and Technology, Nanjing, Jiangsu Province 210019, China
[3]Jiangsu Key Laboratory of Spectral Imaging & Intelligent Sense, Nanjing University of Science and Technology, Nanjing, Jiangsu Province 210094, China
[4]Terahertz Technology Innovation Research Institute, University of Shanghai for Science and Technology, Shanghai 200093, China
[5]School of Computer and Electronic Information, Nanjing Normal University, Nanjing, Jiangsu Province 210023, China
[6]Department of Biomedical Engineering, University of Connecticut, Storrs, Connecticut 06269, USA.
[*]guoan.zheng@uconn.edu
[*]chenqian@njust.edu.cn
[*]zuochao@njust.edu.cn
[†]Equal contribution

## ABSTRACT

This document provides supplementary information for “Adaptive optical quantitative phase imaging based on annular illumination Fourier ptychographic microscopy”. We discuss in detail the pupil updating formula and optimal illumination configuration design of the proposed AO-QPI.

## Contents

## Supplementary Note 1. Pupil function updating formula analysis in FPM

Due to the redundancy of the acquired raw dataset in FPM[1], the pupil of the system can be additionally recovered to realize the imaging aberration correction. At present, the method of EPRY[2] is probably the most common method for the pupil recovery in FPM[3–5]. In this method, the object spectrum and the pupil function are treated as two equivalent variables, which are updated alternatively in the same way. The updating formula of the pupil function is provided in Eq. S1,

$$P = P + \beta \frac{|O|^2}{|O|^2_{max}} \frac{O^*}{|O|^2} [\Phi_u - \Phi_e] \tag{S1}$$

where, O is the spectrum of the specimen, P is the pupil function of the optical system, $\Phi_u$ and $\Phi_e$ are the spectrum with and without the intensity constraint, and $\alpha$ is the updating step size. It should be noted that the method of EPRY is a kind of extended ptychographic iterative engine (ePIE)[6], which was initially used for the probe function recovery. Ptychography[7,8] and FPM differ in that the aperture scanning process in ptychography is in the spatial domain and the intensity images are captured in the frequency domain, which is the exact opposite of FPM. Therefore, if adopting the same non-linear optimization approach, the obtained updating formulas of the two technologies are also identical. However, there is still a problem for such an ePIE method to be applied in FPM, which has not been pointed out before. For ptychography, the weighting term $|O|^2/|O|^2_{max}$ plays a role to defy the detector noise in the updating formula of Eq. S1. However, in the similar scenario of FPM, the object function $O$ is transferred to the frequency domain. Due to the extremely high energy of the DC component in the bright-field spectrum, the most of the pixels in the weighting term $|O|^2/|O|^2_{max}$ are close to zero, resulting in the pupil function $P$ not being effectively updated in reconstruction. Therefore, It should be noted that Eq. S1 is only applicable for the update using the dark-field images. To solve this problem, we choose to resize the exponential factor of the term $|O|/|O|_{max}$ to reduce its dynamic range and improve the convergence of the algorithm . As shown in the revised formula Eq. S2, we set the exponential factor to zero.

$$P = P + \beta \frac{O^*}{|O|^2} [\Phi_u - \Phi_e] \tag{S2}$$

To further verify the forementioned points, we provide the results which were separately reconstructed with the two formulas as shown in Fig. S1. Figure S1(a1) is the input aberration to simulate a possible wave front error in imaging process. Figure S1(a2) is the input phase to represent a typical adherent living cell with large amount of low-frequency information and few high-frequency details. We first performed the reconstruction with the updating formula of Eq. S1 using 81 bright-field (BF) images and 40 dark-field (DF) images (the frequency distribution of the corresponding LED elements are shown in Fig. S1(b1)). The aberration could be successfully recovered in this condition (see Fig. S1(b2) and S1(b3)). Because there is almost no DC component in DF spectrums, the pupil function can be effectively updated by the DF images using the formula of Eq. S1. While if we exclude the DF images in reconstruction as shown in Figs. S1(c1)-S1(c3), the aberration is failed to be characterized and only few pixels are updated [see the

zoomed-in area of Fig. S1(c2)], which is consistent with we have expected before. The recovered phase in Fig. S1(c3) is hence aberrated as well. Figures S1(d1)-S1(d3) demonstrate the results reconstructed with the updating formula of Eq. S2 using 81 BF images and the obtained results are identical to the input. It indicates that pupil function is effectively updated by BF images in reconstruction through the revised formula. In addition, the reconstruction process is also reflected on the aberration error (RMSE) convergence line chart in Fig. S1(e). For the case that 81BF + 40DF images are reconstructed with the Eq. S1, because only DF images work for the aberration recovery, the RMSE descends slowly and converges after about 100 iterations. If the DF images are excluded and only BF images are adopted in reconstruction, the pupil cannot be effectively updated and the RMSE hence remains almost constant. When the adopted pupil updating formula is replaced with Eq. S2, it can seen that the RMSE descends rapidly and achieve the correct solution after about 10 iterations. Through the simulation studies, we have verified that such a revision for the existing updating formula is quite necessary for the correct recovery of the pupil function in FPM.

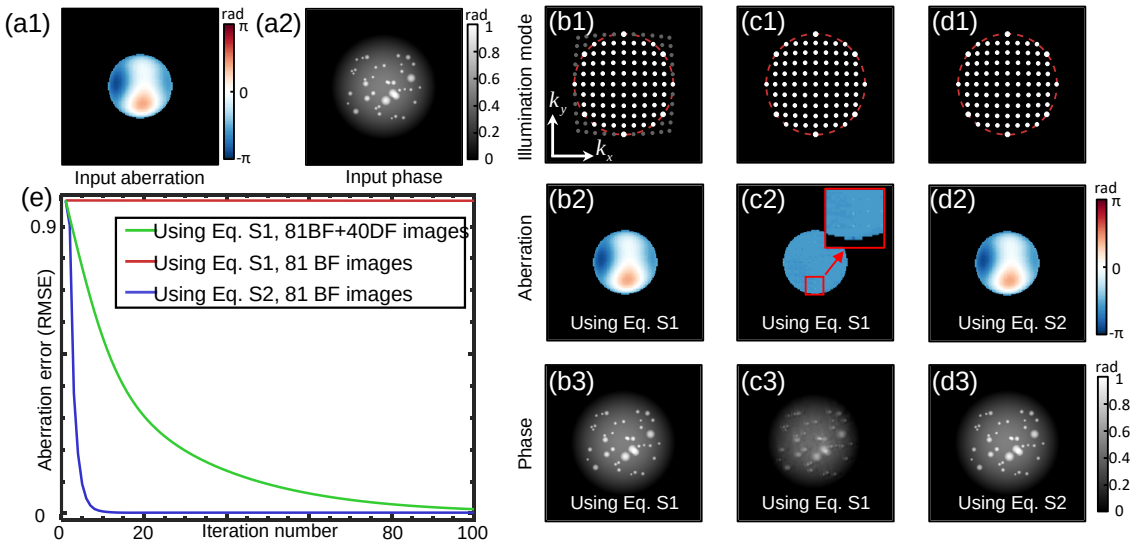


**Figure S1.** The comparison of the reconstructed results using the updating formula of Eq. S1 and Eq. S2. (a1) (a2) Input aberration and input specimen phase of the simulation. (b1)-(b3) The reconstructed results using the updating formula Eq. S1 with 81BF + 40DF images. (c1)-(c3) The reconstructed results using the updating formula Eq. S1 with 81 BF images. (d1)-(d3) The reconstructed results using the updating formula Eq. S2 with 81 BF images. (e) The convergence curves of the aberration error reconstructed under the 3 conditions above.

## Supplementary Note 2. Comparison of aberration recovery with annular illumination and array illumination

In a typical FPM setup, a programmable LED array is usually adopted as the illumination source to provide plane waves from different incident angles. Therefore, the array illumination is the most commonly used illumination mode in FPM. However, it has been verified that the annular illumination mode can equally realize the correct reconstruction of the specimen[9], greatly reducing the number of the captured raw images. Here, we will further demonstrate that the annular illumination could also provide an efficient aberration correction scheme as shown in Fig. S2. Figures (a1)(a2) are the input imaging aberration and specimen phase in the simulation study. We first adopted a typical FPM illumination configuration (see Fig. S2(c1)) and 121 (81BF+ 40DF) raw images are used for the reconstruction. With the sufficient data redundancy, the simulated aberration is correctly solved as shown in Fig. S2(c2). In Fig. S2(d1), we excluded all the DF images and only used BF images for reconstruction. The obtained result is shown in Fig. S2(d2) which is identical to Fig. S2(c2). It indicates that the DF images could not provide additional information for aberration characterization, although it is essential for the resolution enhancement when reconstructing a specimen. The convergence curves under the two conditions are also almost identical as shown in Fig. S2(b). Moreover, in the practical experiments, it is not recommended to adopt DF images for aberration recovery due to its characteristic of low SNR. In Fig. S2(e1), we further excluded most of images and only adopted 12 BF images satisfying the NA-matched illumination condition to complete the reconstruction. The recovered aberration in Fig. S2(e2) indicates that such a sparse illumination configuration could equally provide sufficient information for the complete characterization of imaging aberration. In addition, it can be seen from the Fig. S2(b) that the aberration error of 12 raw images descend relatively slower but it is actually more efficient for the calculation in this condition because much fewer images are used for each iteration.

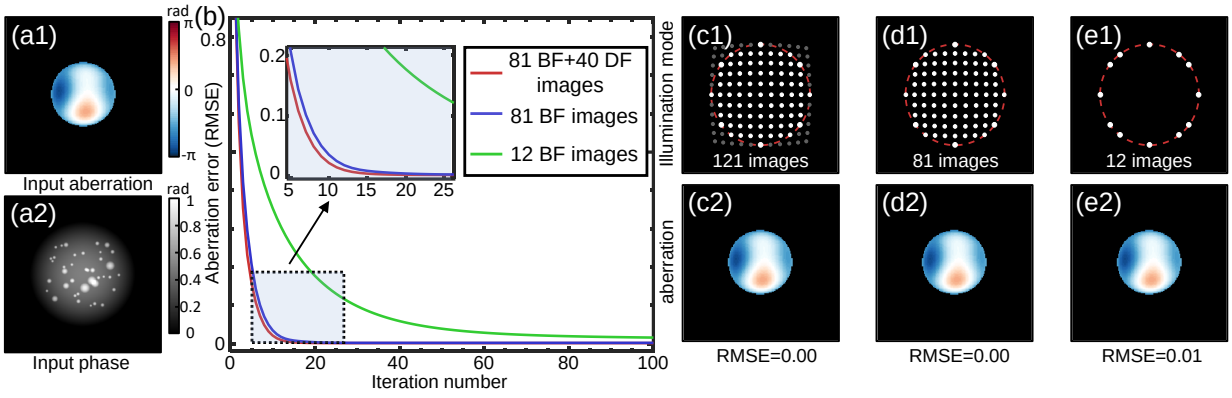


**Figure S2.** The comparison of the reconstructed results with 81 BF + 40 DF images, 81 BF images and, 12 BF images under the matched illumination. (a1) (a2) Input specimen phase and input imaging aberration of the simulation. (b) The convergence curves of the aberration error under the three illumination modes. (c1) (d1) (e1) The LED elements distribution of the three illumination modes. (c2) (d2) (e2) The reconstructed imaging aberrations of the three illumination modes.

## Supplementary Note 3. Significance of NA-matched illumination condition

In the last section, we have verified that the accurate aberration recovery could be achieved only through few raw images based on the annular illumination. However, it should be noted that the key to realize such an efficient recovery is the NA-matched illumination configuration. Here, we further demonstrate the necessity of NA-matched illumination for aberration recovery through simulation studies. We perform the simulation of aberration recovery with the input aberration in Fig. S3(a1) and input specimen phase in Fig. S3(a2) and S3(a3). We adopted two kinds of specimen as the input phase for the reconstruction, because it is found that the frequency characteristic of the specimen is a non-negligible factor that could affect the characterization of the aberration. To fairly compare the aberration recovery results with and without the NA-matched illumination configuration, we perform the reconstruction using the same number of raw images, but with different illumination angles ($NA_{ill} = NA_{obj}, 0.75NA_{obj}, 0.5NA_{obj}$). The convergence curves as well as the reconstructed aberrations are given in Figs. S3(c1)-S3(c4) and Figs. S3(d1)-S3(d3). It can be seen that the ideal solution of the aberrations are achieved under the NA-matched illumination condition, as we have demonstrate in the last section. While if the adopted illumination angle gets smaller than NA of the objective lens, the reconstructed aberrations tend to be unreliable and the aberration error cannot converge to nearly zero. Even though the obtained aberration in figure S3(C3) seems close to the input of the simulation, the value of RMSE shows that there is still a gap with the completely correct solution. In addition, it can be found that the aberration is easier to be recovered with the complicated specimen (Input phase 1) having some high-frequency information. Under the same unmatched illumination condition, the reconstructed aberration in Fig. S3(c3) is obviously closer to the correct solution than in Fig. S3(d3). This is why a speckled diffuser is generally used for digital calibration of aberrations[10]. While if the input specimen phase is a micro lens (Input phase 2) only composed of low-frequency information, the aberration is completely uncharacterized with the unmatched illumination condition. Because in this case, the low-frequency phase information is cancelled[9] and hence almost no information of the aberration is transferred into the intensity contrast recorded by CCD. In conclusion, the NA-matched illumination configuration provides a reliable scheme for imaging aberration characterization, which could work for the specimen of any frequency characteristic to satisfy the practical application scenarios.

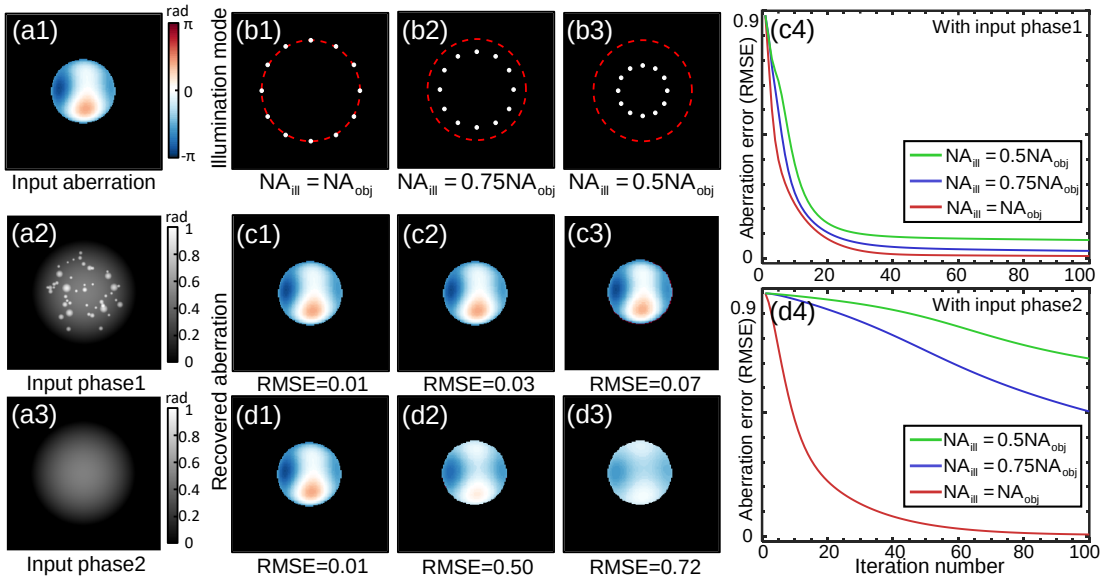


**Figure S3.** The comparison of the reconstructed results under annular illumination of different angles. (a1)-(a3) Input specimen phase and input aberration of the simulation. (b1)-(b3) The annular illumination modes of the LED with different angles. (c1)-(c3) The reconstructed aberrations corresponding to the LED illumination modes in (b1)-(b3) with input phase 1. (d1) -(d3) The reconstructed aberrations corresponding to the LED illumination modes in (b1)-(b3) with input phase 2. (c4) (d4) The convergence curves of the aberration error.

## Supplementary Note 4. Minimum data redundancy criteria for aberration correction

As a typical ill-posed inverse problem, the key for a successful reconstruction in FPM is the sufficient data redundancy[11,12]. Considering the additional reconstruction of the system pupil, it can be speculated that the requirement for data redundancy is even more demanding. Here, to realize aberration correction with a high imaging efficiency, the minimum data redundancy criteria for a successful aberration characterization in FPM is further discussed. Based on the forementioned NA-matched illumination configuration, we reconstruct the pupil aberration with different numbers of raw image in simulation, as shown in Fig. S4. Figures S4(a1) and S4(a2) are the input aberration and input specimen phase of the simulation. In Figs. S4(c1)-S4(c4), we provide the convergence curves as well as the reconstructed aberrations with different number of raw images. It can be seen that at least 9 images are required for the accurate aberration recovery using the method of EPRY[2]. As the number of raw images is reduced to less than 9, the significant artifacts appear on the reconstructed results thus degrading the accuracy of the aberration characterization. Meanwhile, adopting more raw images will only accelerate the convergence of the algorithm but will not improve the reconstructed results. Compared with only using 4 images to realize the phase retrieval[13], it is understandable that approximately double of the data (9 images) are required for the additional recovery of the pupil function, which is solved as a variable with the same degree of freedom as the object function in reconstruction. However, a significant difference between the pupil and the object is that the pupil has unique physical characteristic, which could be exploited to provide prior information for the reconstruction. Therefore, we enforce two constrains placed on the solution of the pupil function. First, the transmittance of the pupil function is assumed uniform across the whole pupil disk with a value of unity. Second, the pupil phase values should be characterized with the use of the narrow-band Fourier optics model. Here, we adopt Zernike polynomials[14,15] as a suitable basis to express the pupil phase,

$$P(u) = circ(\frac{u}{NA/\lambda})e^{i\sum_n^{21} k_n Z_n(u)} \tag{S3}$$

where $circ(u/(NA/\lambda))$ denotes a low-pass filter with a radius of $NA/\lambda$. The aberration of the pupil function is represented by $\sum_n^{21} k_n Z_n(u)$, the weighted sum of the first 21 modes of Zernike polynomial, where $k_n$ is the coefficient and $Z_n(u)$ is the Zernike polynomial of the $n$th mode. By introducing such a Zernike mode constraint, the pupil function is characterized by several coefficients rather than a matrix, which is beneficial to the correct convergence with limited raw images. Figures S4(d1)-S4(d3) are the results reconstructed with the Zernike mode constraint, where the correct convergence of the pupil function can be achieved with only 6 raw images. Through the comparison between Fig. S4(c4) and S4(d4), we can see that the aberration error (RMSE) could converge to a smaller value if imposing the Zernike mode constraint on the pupil function, with the same number of raw images. It indicates that by imposing such a constraint, the aberration can be characterized more accurately with a limited number of raw images. Consequently, by utilizing the Zernike mode constraint and the annular NA-matched illumination configuration, only 6 images could realize the aberration correction for FPM reconstruction.

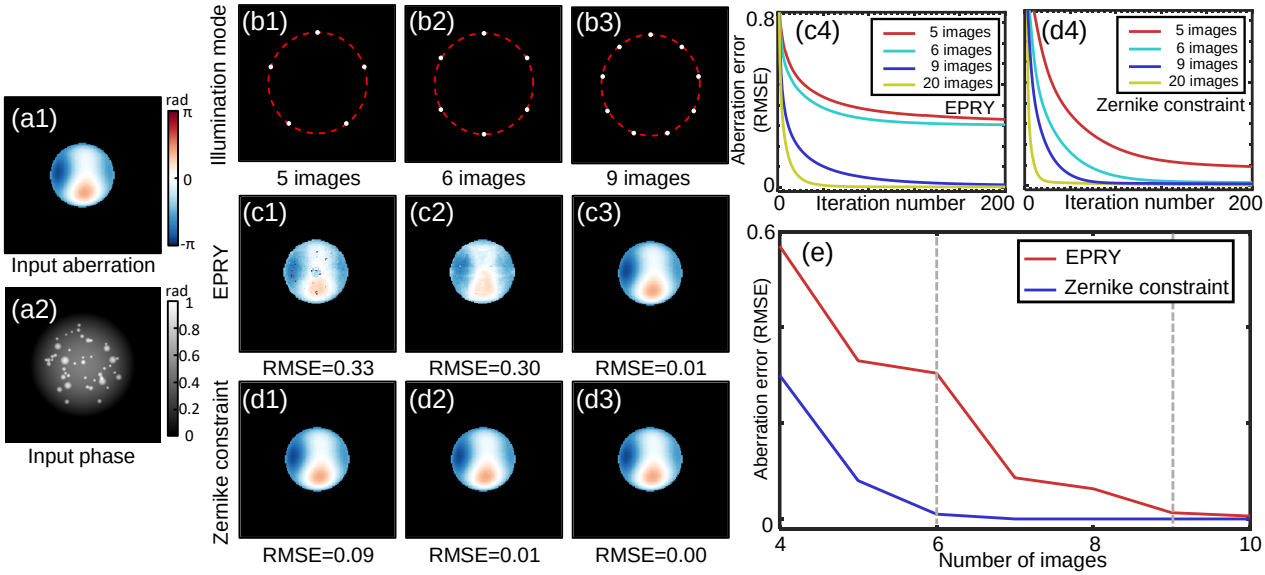


**Figure S4.** The comparison of the reconstructed results under the annular matched illumination with different number of images. (a1) (a2) Input specimen phase and input aberration of the simulation. (b1)-(b3) The illumination modes under the matched illumination with different numbers of LED. (c1)-(c3) The reconstructed aberrations corresponding to the LED illumination modes in (b1) -(b3) using the algorithm of EPRY. (d1)-(d3) The reconstructed aberrations corresponding to the LED illumination modes in (b1)-(b3) using the algorithm of Zernike constraint. (c4) (d4) The convergence curves of the aberration error with different number of images using the algorithms of EPRY and Zernike constraint. (e) The line chart of recovered aberration error (RMSE) with different numbers of images.

## References


1. Zheng, G., Horstmeyer, R. & Yang, C. Wide-field, high-resolution fourier ptychographic microscopy. *Nat. Photonics* **7**, 739–745 (2013).

2. Ou, X., Zheng, G. & Yang, C. Embedded pupil function recovery for fourier ptychographic microscopy. *Opt. Express* **22**, 4960–4972 (2014).

3. Konda, P. C., Taylor, J. M. & Harvey, A. R. Multi-aperture fourier ptychographic microscopy, theory and validation. *Opt. Lasers Eng.* **138**, 106410 (2021).

4. Aidukas, T., Eckert, R., Harvey, A. R., Waller, L. & Konda, P. C. Low-cost, sub-micron resolution, wide-field computational microscopy using opensource hardware. *Sci. Reports* **9**, 7457 (2019).

5. Shen, C. *et al.* Computational aberration correction of VIS-NIR multispectral imaging microscopy based on Fourier ptychography. *Opt. Express* **27**, 24923 (2019).

6. Maiden, A. M. & Rodenburg, J. M. An improved ptychographical phase retrieval algorithm for diffractive imaging. *Ultramicroscopy* **109**, 1256–1262 (2009).

7. Rodenburg, J. M. & Faulkner, H. M. L. A phase retrieval algorithm for shifting illumination. *Appl. Phys. Lett.* **85**, 4795–4797 (2004).

8. Rodenburg, J. Ptychography and Related Diffractive Imaging Methods. In *Advances in Imaging and Electron Physics*, vol. 150, 87–184 (Elsevier, 2008).

9. Sun, J., Zuo, C., Zhang, J., Fan, Y. & Chen, Q. High-speed Fourier ptychographic microscopy based on programmable annular illuminations. *Sci. Reports* **8**, 7669 (2018).

10. Gunjala, G., Sherwin, S., Shanker, A. & Waller, L. Aberration recovery by imaging a weak diffuser. *Opt. Express* **26**, 21054–21068 (2018).

11. Dong, S., Bian, Z., Shiradkar, R. & Zheng, G. Sparsely sampled fourier ptychography. *Opt. Express* **22**, 5455–5464 (2014).

12. Sun, J., Chen, Q., Zhang, Y. & Zuo, C. Sampling criteria for fourier ptychographic microscopy in object space and frequency space. *Opt. Express* **24**, 15765–15781 (2016).

13. Sun, J., Chen, Q., Zhang, J., Fan, Y. & Zuo, C. Single-shot quantitative phase microscopy based on color-multiplexed fourier ptychography. *Opt. Lett.* **43**, 3365–3368 (2018).

14. Lakshminarayanan, V. & Fleck, A. Zernike polynomials: a guide. *J. Mod. Opt.* **58**, 545–561 (2011).

15. Song, P. *et al.* Full-field fourier ptychography (ffp): Spatially varying pupil modeling and its application for rapid field-dependent aberration metrology. *APL Photonics* **4**, 050802 (2019).